Open Access

CrossMark

Rational Design of 3D Honeycomb-Like SnS$_2$ Quantum Dots/rGO Composites as High-Performance Anode Materials for Lithium/Sodium-Ion Batteries

Yingge Zhang[1,2†], Yan Guo[1,2†], Yange Wang[1,2†], Tao Peng[1,2], Yang Lu[1,2], Rongjie Luo[1,2], Yangbo Wang[1,2], Xianming Liu[3*], Jang-Kyo Kim[4] and Yongsong Luo[1,2*]

Abstract

Structure pulverization and poor electrical conductivity of metal dichalcogenides result in serious capacity decay both in lithium-ion batteries (LIBs) and sodium-ion batteries (SIBs). To resolve the above problems, a combination of metal dichalcogenides with conductive scaffolds as high-performance electrode materials has aroused tremendous interest recently. Herein, we synthesize a 3D honeycomb-like rGO anchored with SnS$_2$ quantum dots (3D SnS$_2$ QDs/rGO) composite via spray-drying and sulfidation. The unique 3D-ordered honeycomb-like structure can confine the volume change of SnS$_2$ QDs in the lithiation/delithiation and sodiation/desodiation processes, provide enough space for electrolyte reservoirs, promote the conductivity of the SnS$_2$ QDs, and improve the electron transfer. As a result, the 3D SnS$_2$ QDs/rGO composite electrode delivers a high capacity and long cycling stability (862 mAh/g for LIB at 0.1 A/g after 200 cycles, 233 mAh/g for SIB at 0.5 A/g after 200 cycles). This study provides a feasible synthesis route for preparing 3D-ordered porous networks in varied materials for the development of high-performance LIBs and SIBs in future.

Keywords: SnS$_2$ quantum dots, Spray drying, rGO, Lithium-ion batteries, Sodium-ion batteries

Background

Energy storage plays a remarkable role in modern life. Li-ion batteries (LIBs) have been widely applied as a power source for portable electronic devices and power electric vehicles due to their long cycle life stability and high energy density. Meanwhile, Na-ion batteries (SIBs) have attracted tremendous attention in renewable energy storage because of their low cost and environmental benignity. While the commercial graphite anodes of LIBs show low theoretical capacity (372 mAh/g) and suffer from structural instability and safety problem during a high-rate charge-discharge process, also cannot be used in SIBs owing to their small inter-layer space [1–4].

Therefore, novel anode materials with high capacity need to be developed for the next-generation LIBs and SIBs.

Metal dichalcogenides, possessing high theoretical capacities, are promising candidates for replacing the commercial graphite in LIB and SIB applications. Among the metal dichalcogenides, layered SnS$_2$ exhibits a higher theoretical capacity than graphite, and has been regarded as an attractive anode material. SnS$_2$ is a typical CdI$_2$-type, where the each layer connects with each other mainly by weak Van der Waals force. Such a feature makes it a desired intercalation/deintercalation candidate for Li$^+$ and Na$^+$ in the first step of the conversion reaction. However, SnS$_2$ suffers from large volume change and poor electrical conductivity in the charge-discharge process, thus results in severe capacity decay.

Integrating SnS$_2$ with other conductive scaffolds to design a rational structure especially a three-dimensional (3D)-ordered porous network has been considered as feasible strategies to improve the electrical conductivity

* Correspondence: myclxm@163.com; ysluo@xynu.edu.cn
†Yingge Zhang, Yan Guo and Yange Wang contributed equally to this work.
³College of Chemistry and Chemical Engineering, Luoyang Normal University, Luoyang 471934, People's Republic of China
¹School of Physics and Electronic Engineering, Xinyang Normal University, Xinyang 464000, People's Republic of China
Full list of author information is available at the end of the article

Zhang *et al. Nanoscale Research Letters*   (2018) 13:389

Page 2 of 10

and cycling stability of LIBs and SIBs [5, 6]. Graphene is considered a promising candidate for scaffolds owing to its excellent mechanical characteristics and electronic conductivity. Firstly, compared to 1D and 2D structures, a 3D-ordered porous network is more conducive to the complete contact between the electrode and electrolyte. Thus, it can act as a channel for fast electron transport along the 3D direction and restrain the aggregation effectively [7]. Secondly, the rich pores in 3D-ordered porous network can relieve the volume expansion in three dimensions space and thus makes it exhibit long cycle life stability [8–14]. Zhu et al. designed Co_3O_4 with a 3D mesoporous network and showed excellent performance in LIBs [15]. Deng et al. demonstrated a new 3D-ordered macroporous MoS_2/carbon nanostructure is beneficial for obtaining high-performance of LIBs [16]. Choi et al. synthesized layered WS_2 nanosheet-decorated 3D-RGO microspheres as an anode material for SIBs [17]. Based on the above discussion, we have designed a unique 3D honeycomb-like structure to buffer the large volume change and enhance the electrical conductivity of SnS_2 by spray drying and sulfidation. The composite achieves excellent electrochemical performance in both LIBs and SIBs (862 mAh/g for LIB at 0.1 A/g after 200 cycles, 233 mAh/g for SIB at 0.5 A/g after 200 cycles).

The 3D-structured honeycomb-like rGO anchored with SnS_2 quantum dots composite (3D SnS_2 QDs/rGO) via a two-step method. Firstly, the 3D honeycomb-like rGO anchored with SnO_2 composite (3D SnO_2/rGO) is synthesized through spray drying and post-calcination. Then, it is annealed with thiourea to obtain the 3D SnS_2 QDs/rGO composite under the argon atmosphere. The 3D honeycomb-like structure can reduce the inter-sheet junction contact resistance effectively, provide a large accessible active surface area for the adsorption/desorption of ions, restrain the aggregation of SnS_2 QDs, and buffer the volume expansion of SnS_2 QDs [18–20]. As a result, the SnS_2 QDs with a diameter of ~ 6 nm are uniformly distributed within the rGO layer after 200 charge/discharge cycles in the LIB test. Moreover, the 3D SnS_2 QDs/rGO composite electrode possesses a high capacity and long cycling stability (862 mAh/g for LIB at 0.1 A/g after 200 cycles, 233 mAh/g for SIB at 0.5 A/g after 200 cycles). The unique metal sulfide-based 3D porous graphene materials presented in this study provide a way to the development of high-performance LIBs and SIBs.

Methods

Synthesis of Polystyrene Nanospheres

All reagents used were of analytical grade and were used directly without any purification. Styrene was alternatively washed with DI water and 1 M NaOH to remove the polymer inhibitors. Then, 8 ml styrene, 92 ml DI water, and 0.2 g $K_2S_2O_8$ were mixed and then stirred at 80 °C for 10 h in argon atmosphere. Finally, a white product was obtained by centrifugation. After washed by DI water and ethanol for at least five times, the product was freeze-dried at – 50 °C for 24 h [16].

Fabrication of 3D SnS_2 QDs/rGO Composite

In a typical synthesis, 24 g graphene oxide (GO) colloidal (2.5 wt%) that was obtained by the modified Hummer approach was added into 500 ml DI water. Then, 3 g polystyrene (PS) nanospheres were dispersed in the prior solution [21, 22]. Further, 1.5 g tin (IV) chloride pentahydrate ($SnCl_4 \cdot 5H_2O$) was placed into the mixture and ultra-sonication for 1 h. The mixture solution was spray-dried with exit temperature of 140 °C and a flow rate of 800 ml/h. Subsequently, the collected product was annealed at 450 °C for 2 h at a ramping rate of 3 °C min^{-1} in Ar atmosphere to remove PS nanospheres, and then the 3D SnO_2/rGO was obtained. Finally, thiourea, acting as the sulfur source, was mixed with the SnO_2/rGO. And then it was annealed at 350 °C for 12 h at a heating rate of 2 °C min^{-1} in Ar atmosphere to ensure the 3D SnO_2/rGO composite completely transformed into 3D SnS_2 QDs/rGO composite [23]. The pure SnS_2 composite was synthesized in the absence of GO and PS nanospheres.

Characterization

The crystalline structure and phase of the composites were tested by X-ray diffraction (XRD, D8-Advance Bruker) with Cu-Kα ($\lambda = 1.5418$ Å) radiation at 40 kV and 40 mA, ranging from 10 to 80 °C at room temperature. The surface chemical composition of the composites was analyzed by a modified X-ray photoelectron spectroscopy (XPS, PHI 5600). The morphologies and structures were examined by field emission scanning electron microscope (FESEM, JEOL S-4800) and transmission electron microscope (TEM, JEOL JEM-2010). The Brunauer–Emmett–Teller (BET) surface area and pore size were identified by using the nitrogen adsorption/desorption isotherms obtained at 77 K on a surface area and porosity analyzer (Quadrasorb SI-MP, Quantachrome). The Raman spectrum was obtained by an INVIA Raman microprobe (Renishaw Instruments) with a 532 nm laser source and a × 50 objective lens. The thermogravimetric analyzer (TGA) curve was performed using an STD Q600 TA with 100 ml min^{-1} of air flow from 30 to 800 °C at a heating rate of 10 °C min^{-1}.

Electrochemical Test

To prepared working electrodes, 70 wt% 3D SnS_2 QDs/rGO composite, 20 wt% acetylene black, and 10 wt% polyvinylidene fluoride were mixed and dissolved in *N*-methyl-2-pyrrolidinone. After stirring for 5 h, the

Zhang *et al. Nanoscale Research Letters* (2018) 13:389

Page 3 of 10

obtained slurry was coated onto the copper foil (acted as a current collector) and dried at 80 °C in vacuum overnight. The electrochemical tests were carried out using two-electrode cells assembled in an argon-filled glove box. Li and Na metals acted as the counter electrode. The organic electrolyte in LIBs was constituted of 1.0 M $LiPF_6$ in ethylene carbonate (EC) and diethyl carbonate (DEC) (1:1, v/v). For SIBs, the electrolyte was 1 M $NaClO_4$ in a mixture of EC/DEC (1:1, v/v). Galvanostatic charge/discharge measurements were performed by a battery test system (NEWARE, Shenzhen Xinwei Electronics, Ltd) at different current densities with a voltage range of 0.01–3.00 V. Cyclic voltammetry (CV) and the cyclic voltammograms were recorded over the potential range of 0.01–3.00 V with a scan rate of 0.1 mV/s.

Results and Discussion

Scheme 1 illustrates the synthesis process of the 3D SnS_2 QDs/rGO composite. A colloidal solution, consisting of uniformly dispersed GO nanosheets, PS nanospheres, and tin (IV) chloride pentahydrate is stirred for 6 h at room temperature. To ensure that no precipitate is formed, the colloidal solution is made to stand for several hours before being nebulized. Subsequently, the Sn salt-GO-PS composite is formed inside the reactor in 10 s (Fig. 1a). Second, the 3D SnO_2/rGO composite is synthesized through calcination in Ar atmosphere, as shown in Additional file 1: Figures S1a and S1b. During the formation of the 3D SnO_2/rGO composite, the PS nanospheres with a mean size of 200–300 nm act as a sacrificed template is uniformly anchored on the rGO layers. After calcination, the decomposition of the PS

nanospheres results in 200–300-nm-sized voids, lead to the formation of a 3D honeycomb-like structure, as shown in Additional file 1: Figure S1c. Finally, thiourea is used as the sulfur source and reductant to react with the precursor 3D SnO_2 /rGO to obtain honeycomb-like 3D SnS_2 QDs/rGO composite (Fig. 1b, c). The TEM image in Fig. 1d further demonstrates the 3D honeycomb-like structure, which is consistent with the morphology presented in the SEM images. Moreover, the thinned layers of rGO nanosheets of the 3D SnS_2 QDs/rGO composite can be clearly observed in the TEM image shown in Additional file 1: Figure S1d. The ultrafine SnS_2 QDs with several nanometers in size is distributed within the 3D rGO layers while compared Figs. 1e, f with Additional file 1: Figure S1d. The enlarged TEM image of the SnS_2 QDs showed in Fig. 1f indicates clear lattice fringes separated by 0.32 nm, which correspond to the (100) plane of SnS_2. The distribution of Sn, S, and C in the composite was uniform as shown in Fig. 1g–j.

The XRD patterns of rGO and the 3D SnS_2 QDs/rGO composite are shown in Fig. 2a. The rGO presents three diffraction peaks at 2θ = 15.04°, 26.14°, and 44.52°. The first peak belongs to the characteristic peak of GO, which is further verified by the following Raman spectrum. The next two peaks are attributed to the (002) and (100) lattice planes of the hexagonal graphene (JCPDS No. 03-065-2023). The diffraction peaks of 3D SnS_2 QDs/rGO can be observed at 15.0°, 28.2°, 30.26°, 41.9°, 49.96°, 58.35°, and 70.33°, which correspond to the crystal planes (001), (100), (002), (102), (110), (200), and (113) (JCPDS No. 23-0677) of SnS_2, respectively [24].
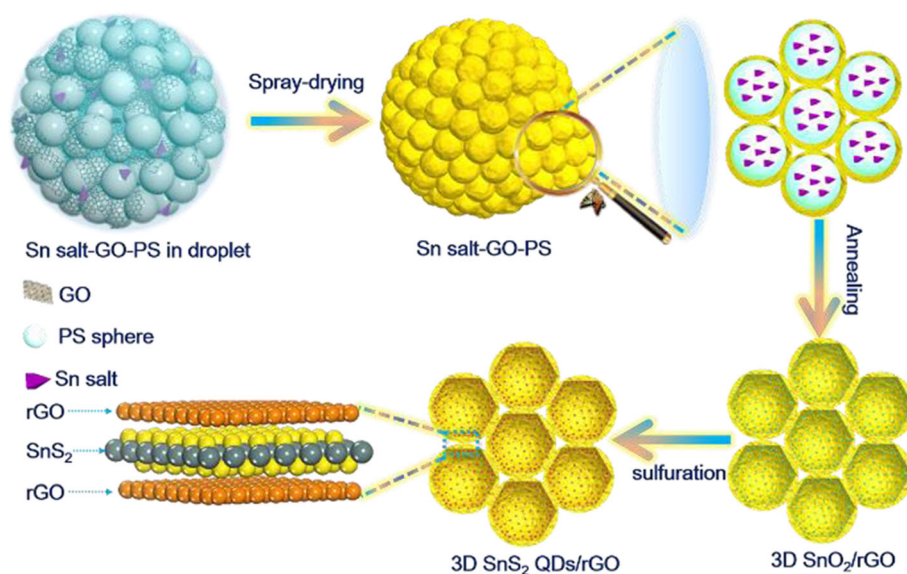
Scheme 1 Schematic of the fabrication of the 3D SnS_2 QDs/rGO composite by spray drying and sulfuration and the interface microstructure model of the SnS_2/rGO composite

Fig. 1 a SEM image of the Sn salt-GO-PS composite. **b** SEM image of the 3D SnS₂ QDs/rGO composite. **c** Photograph of a honeycomb-like structure. **d, e** TEM images of the 3D SnS₂ QDs/rGO composite. **f** HRTEM image of the 3D SnS₂ QDs/rGO composite. **g–j** Elemental mapping images of Sn, S, and C elements
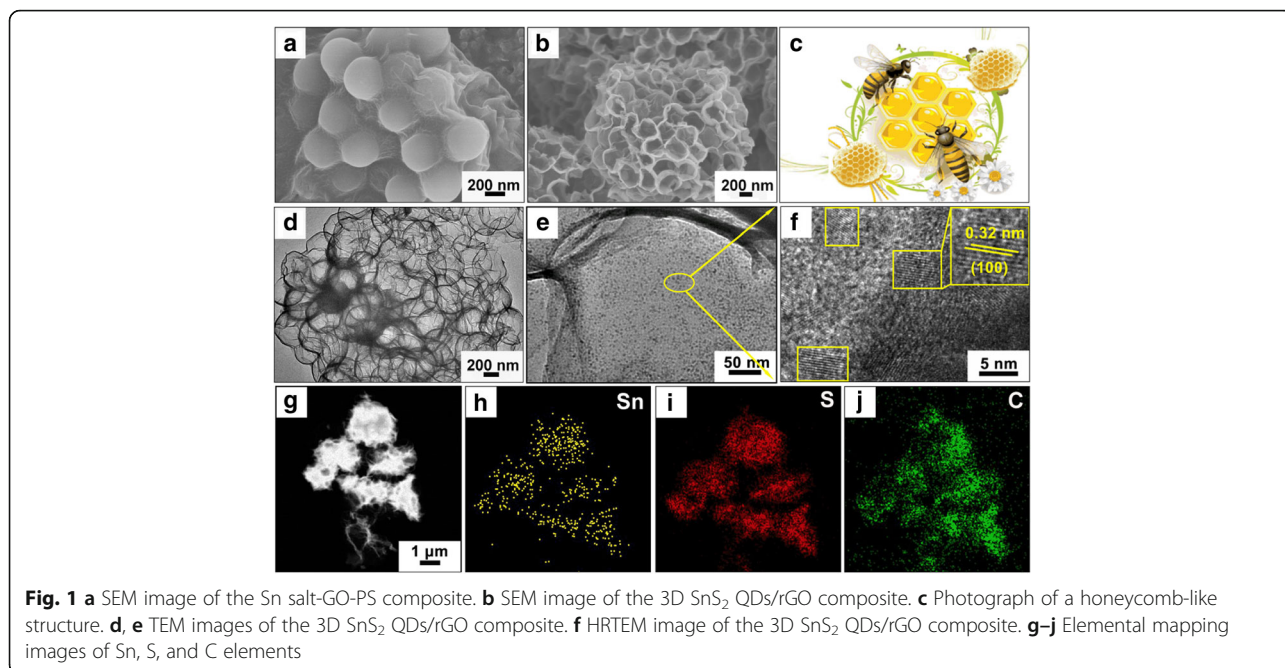
Compared to the pure SnS_2 showed in Additional file 1: Figure S2a, the relatively broad diffraction peaks of the 3D SnS_2 QDs/rGO composite indicate smaller particle sizes, which are in accordance with the TEM results. To further investigate the structure of the 3D SnS_2 QDs/ rGO composite, the Raman spectrums of the composite and rGO are obtained in Fig. 2b. The Raman peaks of rGO that appeared at 1596 and 1348 cm^{-1} are attributed

to the G and D bands of the carbon structure, respectively. Generally, the D band is relevant to the defects of carbon atoms in graphitic layers, while the G band belongs to the stretching vibration of -C=C- in a 2D hexagonal lattice. A much weaker peak appeared at about 309 cm^{-1} in the 3D SnS_2 QDs/rGO composite, which corresponds to the characteristic peak of the A_{1g} mode of the SnS_2 phase [25]. Moreover, the D band observed

Fig. 2 a XRD pattern and **b** Raman spectra of the rGO and 3D SnS₂ QDs/rGO composite. **c** N₂ adsorption–desorption isotherms and the corresponding pore size distributions of the 3D SnS₂ QDs/rGO composite. High-resolution XPS spectra of **d** Sn 3d, **e** S 2p, and **f** C 1 s of the 3D SnS₂ QDs/rGO composite
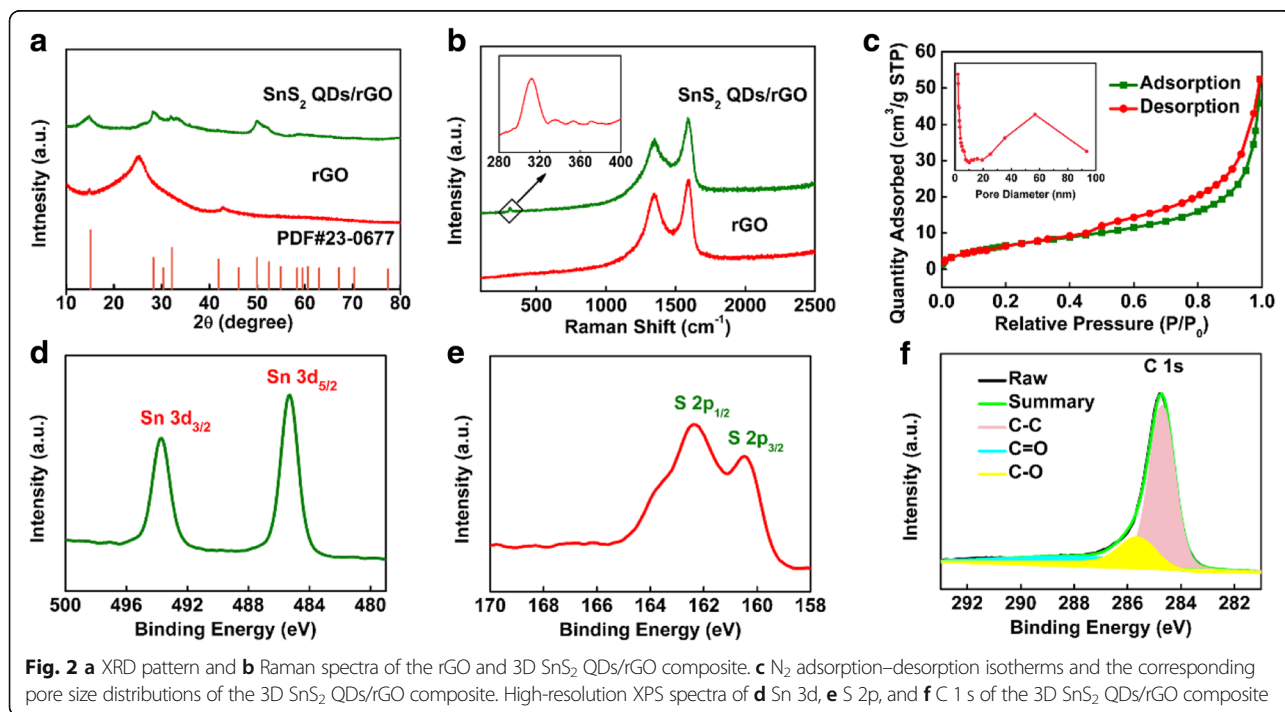
at 1349 cm^{-1} and the G band observed at 1587 cm^{-1} belonged to 3D SnS$_2$ QDs/rGO [26]. While the SnS$_2$ can influence the reduction in GO and hinder its reduction, the composite exhibits a slightly higher intensity in D peak than rGO [27]. Such result can also explain the peak that appears at 2θ = 15.04° in XRD patterns. To investigate the BET surface area and pore size, the internal porosity and microstructure of the as-prepared 3D SnS$_2$ QDs/rGO composite are measured by nitrogen adsorption-desorption measurements. The remarkable hysteresis loops of N$_2$ adsorption-desorption isotherms shown in Fig. 2c can be assigned to the type IV loop, which demonstrates the standard nanoporous structure of the composite. The specific surface area of the composite is calculated to be 21.99 m^2 g^{-1} by using a multi-point BET method according to the adsorption branch of the isotherm. As a consequence, the 3D SnS$_2$ QDs/rGO composite with such a pore structure can provide more active sites and is conducive to the ion diffusion in the charge/discharge process [28, 29].

The surface chemical composition and oxidation state of the composite are analyzed by XPS system. In Fig. 2d, the two prominent peaks at 487.3 and 495.7 eV are ascribed to Sn 3d$_{3/2}$ and Sn 3d$_{5/2}$, respectively. The energy difference between Sn 3d$_{5/2}$ and Sn 3d$_{3/2}$ is 8.4 eV, which indicates the Sn^{4+} oxidation state [30]. The survey XPS S

2p spectrum is presented in Fig. 2e. The characteristic peaks appearing at 161.3 and 163.4 eV are attributed to S 2p$_{3/2}$ and S 2p$_{1/2}$ for S^{2-} in SnS$_2$ [27, 31]. The XPS spectrum of C 1s showed in Fig. 2f can be fitted and split into three different peaks of 284.7, 285.7, and 288.1 eV, respectively. The three peaks belonged to the C-C, C-O, and C=O bonds, respectively [25, 32].

The mass percentage of SnS$_2$ in 3D SnS$_2$ QDs/rGO composite was conducted by TGA from 30 to 800 °C at a heating rate of 10 °C/min in air. In Additional file 1: Figure S4a, the 3D SnS$_2$ QDs/rGO composite was completely oxidized to SnO$_2$ over 800 °C, producing a total weight loss of about 29.5%. The process of weight loss contained three processes, namely the desorption of water molecules (1.4%) adsorbed on the 3D SnS$_2$ QDs/rGO composite, oxidization of SnS$_2$, and the successively burning of rGO. The weight percentages of SnS$_2$ in the 3D SnS$_2$ QDs/rGO composite can be calculated to be 83.7%, based on the complete weight loss of rGO combustion and the partial weight loss from the transformation of SnS$_2$ into SnO$_2$ [28].

To investigate the lithium storage processes of the 3D SnS$_2$ QDs/rGO and the pure SnS$_2$ as anode materials for LIBs, their CV curves are tested at a scan rate of 0.1 mV/s, as shown in Fig. 3a, b. In Fig. 3a, the reduction peaks at 1.0–1.5 V are attributed to phase decomposition, structure
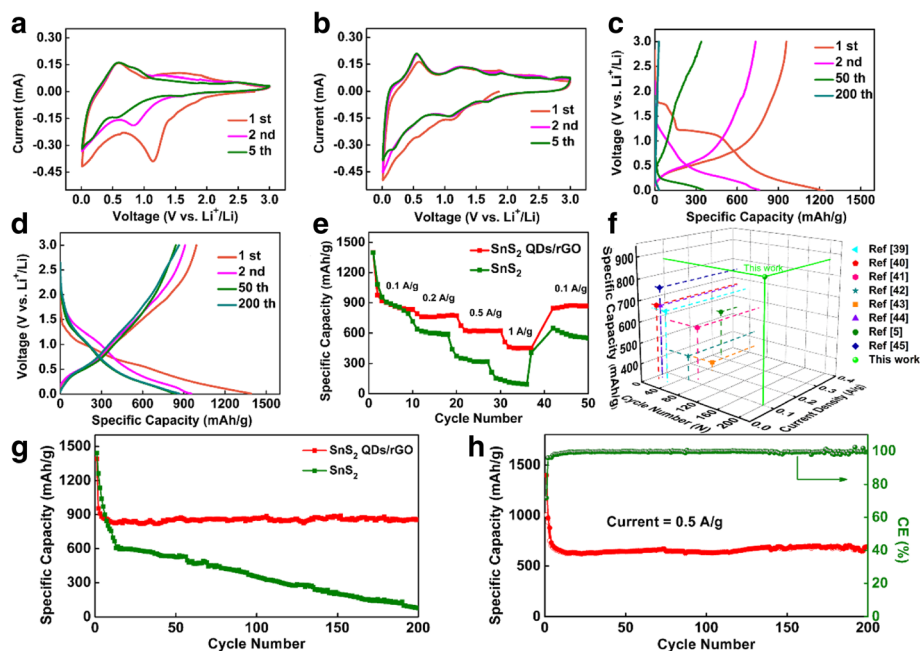
Fig. 3 Electrochemical performance of the pure SnS$_2$ and 3D SnS$_2$ QDs/rGO composite electrodes for LIBs: **a**, **b** CV curves of the pure SnS$_2$ and 3D SnS$_2$ QDs/rGO composite electrodes at a scan rate of 0.1 mV/s for the first five cycles. **c** Charge/discharge curves of the pure SnS$_2$ composite electrode and **d** the 3D SnS$_2$ QDs/rGO composite electrode at a current density of 0.1 A/g in the voltage range of 0.01–3.0 V vs. Li$^+$/Li. **e** Rate performance of the 3D SnS$_2$ QDs/rGO and pure SnS$_2$ composite electrodes at rates ranging from 0.1 to 1 A/g. **f** Comparison of electrochemical performance between the 3D SnS$_2$ QDs/rGO composite (the current study) and previously reported SnS$_2$-based material composite. **g** Cycling performances of 3D SnS$_2$ QDs/rGO and pure SnS$_2$ composite electrodes at a current density of 0.1 A/g. **h** Cycling performance and Coulombic efficiency of 3D SnS$_2$ QDs/rGO composite electrode at a current density of 0.5 A/g

Zhang *et al. Nanoscale Research Letters* (2018) 13:389

Page 6 of 10

collapse, and formation of a solid electrolyte interface (SEI) layer. In Fig. 3b, the first reduction peak at 1.7 V is assigned to the intercalation of Li$^+$ into the SnS$_2$ nanostructure during the first cycle [33]. The second reduction peak at 1.1 V is attributed to the decomposition of SnS$_2$ QD to metallic Sn and Li$_2$S (as shown in reaction (1)) [34]. The third reduction peak below 0.5 V indicates the appearance of Li$_x$Sn alloys according to reaction (2) and the Li$^+$ inserted into the rGO layered nanostructure [35, 36]. During reverse scanning, the first oxidation peak at 0.52 V indicates the de-alloying of Li$_x$Sn according to reaction (2). The second oxidation peak at 1.8 V can be attributed to the fact that the Li$_2$S can decompose partly and the Sn can be oxidized to Sn^{4+} (see the reverse reaction (1)) [34, 37, 38]. The reactions of the above mentioned are as follows:

$$SnS_2 + 4Li^+ + 4\,e^- \rightarrow 2Li_2S + Sn \qquad (1)$$

$$Sn + x\,Li^+ + xe^- \leftrightharpoons Li_xSn\ (0 \leq x < 4.4) \qquad (2)$$
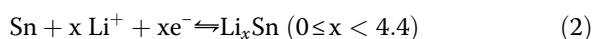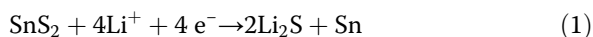
Note that the intensities of the reduction peaks of SnS$_2$ decrease drastically in the second and fifth scans. In contrast, the reduction peaks of the 3D SnS$_2$ QDs/rGO electrode perfectly overlap in the second and fifth scans, suggesting its excellent electrochemical reversibility and stability.

Galvanostatic charge/discharge measurements of the pure SnS$_2$ and 3D SnS$_2$ QDs/rGO electrodes are also performed at a current density of 0.1 A/g between 0.01 and 3.00 V vs Li$^+$/Li. The charge/discharge curves (1st, 2nd, 50th, and 200th cycles) are shown in Fig. 3c, d, respectively. In Fig. 3c, the charge/discharge curve of the pure SnS$_2$ electrode shows a drastic decrease to 16 mAh/g after the 200th cycle. In Fig. 3d, the initial discharge capacity for the 3D SnS$_2$ QDs/rGO electrode is 1400 mAh/g. It is higher than the theoretical storage capacity of Li$^+$ (1231 mAh/g) of SnS$_2$ calculated from both reactions (1) and (2) according to the Faraday equation. This is ascribed to the formation of a SEI layer on the surface of the 3D SnS$_2$ QDs/rGO electrode caused by the irreversible insertion of Li$^+$ and the decomposition of the electrolyte [3]. Upon increasing the cycles to 2, 50, and 200, the capacities of the 3D SnS$_2$ QDs/rGO electrode are maintained at 975, 867, and 870 mAh/g, respectively. Obviously, the 3D SnS$_2$ QDs/rGO electrode possesses an excellent charge/discharge stability and long cycle life than the pure SnS$_2$ electrode.

The rate performances of the electrodes are presented in Fig. 3e. It can be seen that the discharge capacity at a rate of 0.1, 0.2, 0.5, and 1 A/g is 870, 770, 622, and 452 mAh/g, respectively. Then it easily return to 867 mAh/g at 0.1 A/g, indicating that the 3D SnS$_2$ QDs/rGO composite can bear gradual rate variations and possesses remarkable electrochemical stability and

reversibility. While the pure SnS$_2$ electrode' capacity decays to 792, 587, 319, and 106 mAh/g with the discharge/charge rates increased to 0.1, 0.2, 0.5, and 1 A/g, respectively. And it only restores to 662 mAh/g when the discharge/charge rate is recovered to 0.1 A/g. The outstanding electrochemical performance of 3D SnS$_2$ QDs/rGO composite electrodes is further presented in Fig. 3g. The capacity of the pure SnS$_2$ electrode drastically decreases to almost 16 mA/g after 200 cycles, while the 3D SnS$_2$ QDs/rGO electrode can still maintain a value of 870 mAh/g after 200 cycles at a current density of 0.1 A/g. Moreover, in Fig. 3h, the test is performed to prove the better cycling performance of the composite at a scan rate of 0.5 A/g. After 200 charge/discharge cycles, a high reversible capacity of 622 mAh/g remained and the average Coulombic efficiency is as high as 99.44%.

To further understand the better cycle life of the 3D SnS$_2$ QDs/rGO electrode, a TEM image is acquired to prove the distribution of the SnS$_2$ QDs (in Additional file 1: Figure S3, by measuring 100 representative particles using the Nano-Measure software). The SnS$_2$ QDs with ~ 6 nm are almost evenly anchored and limited within the rGO layers, indicating a strong adsorption between SnS$_2$ QDs and the rGO layers. Overall, the results of both the electrochemical test and the particle distribution demonstrate that the introduction of rGO and the 3D honeycomb-like network offers abundant void spaces for volume expansion of SnS$_2$ QDs. These structures act as channels for fast transportation of electron along all three directions and effectively restrain the aggregation. Thus, the rate performance and cycling stability of the composite are enhanced. Figure 3f shows a comparison of the electrochemical performance between the 3D SnS$_2$ QDs/rGO composite (the current study) and the previously reported SnS$_2$-based materials composite. It can be observed that the capacity of 3D SnS$_2$ QDs/rGO in our study remains 862 mAh/g LIB at 0.1 A/g after 200 cycles, which is higher than the other rGO and SnS$_2$-based material, such as graphene-SnS$_2$ hybrids [39], acetylene black-SnS$_2$ [40], SnS$_2$@reduced graphene oxide [41], mesoporous carbon anchored with SnS$_2$ nanosheets [42], graphene-SnS$_2$ [43], SnS$_2$ nanoparticle-loaded grapheme [44], SnS$_2$@graphene [5], and Ultrathin SnS$_2$ nanoparticles on graphene nanosheets [45].

To investigate the sodium storage processes of 3D SnS$_2$ QDs/rGO and pure SnS$_2$ as anode materials for SIBs, cyclic voltammetry is performed at a scan rate of 0.1 mV/s between 0.01 and 3.00 V vs Na$^+$/Na, as shown in Fig. 4a, b. In Fig. 4a, the reduction peak at 0.3–1.0 V is corresponded to the conversion, alloying reactions (Eqs. (4) and (5)), and the formation of the SEI layer in the initial cycle. In Fig. 4b, the rather broad peak at ~

Zhang *et al. Nanoscale Research Letters*   (2018) 13:389

Page 7 of 10
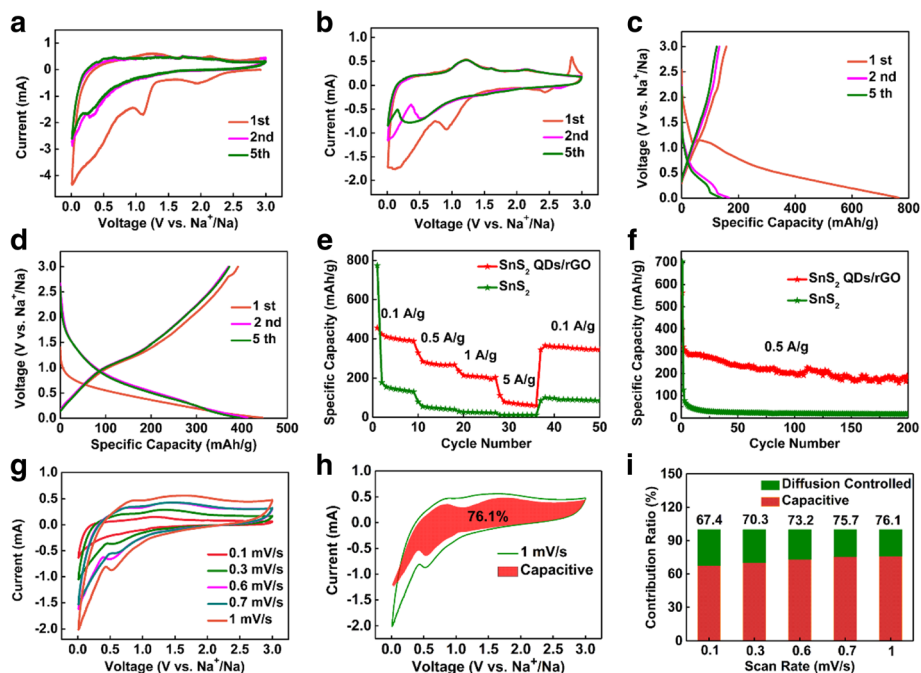
Fig. 4 Electrochemical performance of the pure SnS_2 and 3D SnS_2 QDs/rGO composite electrodes for SIBs. **a**, **b** CV curves of the pure SnS_2 electrode and 3D SnS_2 QDs/rGO composite electrode at a scan rate of 0.1 mV/s for the first five cycles. **c** Charge/discharge curves of the pure SnS_2 composite electrode and **d** the 3D SnS_2 QDs/rGO composite electrode at a current density of 0.1 A/g in the voltage range of 0.01–3.0 V vs. Na^+/Na. **e** Rate performance of 3D SnS_2 QDs/rGO and the pure SnS_2 composite electrode at rates ranging from 0.1 to 5 A/g. **f** Cycling performance of 3D SnS_2 QDs/rGO composite electrode and the pure SnS_2 electrode at a current density of 0.5 A/g. **g** CV curves of 3D SnS_2 QDs/rGO composite electrode at different scan rates. **h** Capacitive contribution at the scan rate of 1 mV/s. **i** Contribution ratio of the capacitive and diffusion-controlled charge vs. different scan rates

1.0 V in the first reduction process is corresponded to the insertion of Na^+ into the SnS_2 layers (analogous to that of Li intercalation) according to Eqs. (3) [46, 47]:

$$SnS_2 + x\,Na^+ + xe^- \rightarrow Na_xSnS_2 \qquad (3)$$

$$Na_xSnS_2 + (4-x)Na^+ + (4-x)e^- \rightarrow Sn + 2Na_2S \qquad (4)$$

$$Sn + xNa^+ + xe^- \rightarrow Na_xSn \qquad (5)$$
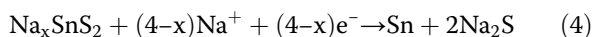
In reverse scanning, the unconspicuous oxidation peaks at 0.35, 1.2, and 2.25 V are ascribed to the desodiation of Na_xSn. The obvious oxidation peak at 1.2 V belongs to the resilience of the initial 3D SnS_2 QDs/rGO electrode [25]. Note that the subsequent CV scans of 3D SnS_2 QDs/rGO overlap well after the first cycle, indicating good reversibility of it for the sodiation and desodiation reactions.

The discharge-charge voltage profiles of the pure SnS_2 and 3D SnS_2 QDs/rGO electrodes are carried out between 0.01 and 3 V at a current density of 0.1 A/g. The corresponding charge/discharge profiles (1st, 2nd, and 5th cycles) are shown in Fig. 4c, d, respectively, which are in accord with the CV results. In Fig. 4c, a remarkable plateau appears at ~ 1.0 V in the discharge process, belonging to the formation of Na_xSnS_2. The plateau at

0.5–1.0 V is attributed to the conversion, while that below 0.5 V is assigned to the alloying reactions between Na^+ and Sn. Then, the CV curve of the 3D SnS_2 QDs/rGO electrode (Fig. 4d) indicates that the inconspicuous plateau voltage at ~ 1.0 V is assigned to the intercalation of Na^+ into SnS_2 layers during the first discharge process and this reaction is expressed as Eq. (3). The slope plateau at 0.3–1.0 V corresponds to the conversion reaction (Eq. (4)), the formation of the SEI layer by the irreversible insertion of Na^+, and the decomposition of the electrolyte. The plateau below 0.3 V corresponds to the alloying reaction (Eq. (5)) [48–50]. The electrode shows a plateau at ~ 1.0 V and a slope plateau at ~ 1.6 V in the charge process, which are also in agreement with the CV results.

The rate capability of the pure SnS_2 and 3D SnS_2 QDs/rGO electrodes from 0.1 to 5 A/g in the SIB test are given in Fig. 4e. The 3D SnS_2 QDs/rGO electrode is remarkably superior by comparison. It can be seen that the discharge capacities at the rate of 0.1, 0.5, 1, and 5 A/g are 397, 286, 213, and 95 mAh/g, respectively, and then easily return to 393 mAh/g at 0.1 A/g. But for the pure SnS_2 electrode, the discharge capacity decays to 180, 59, 25, and 11 mAh/g with the discharge rate increased to 0.1, 0.5, 1, and 5 A/g, respectively. Then the discharge capacity only restores to 102 mAh/g when the

discharge rate recovers to 0.1 A/g. The 3D SnS_2 QDs/rGO electrode shows slight changes in discharge capacity after discharge at different current densities, which indicates better resilience of the nanostructure. Obviously, the unique 3D honeycomb-like structure allows Na^+ transport at high current density without creating many irreversible changes of the electrode's nanostructure, resulting in an excellent performance in SIBs. The discharge capacity of the pure SnS_2 electrode retains only 6 mAh/g after 200 cycles at a scan rate of 0.5 A/g, which is significantly lower than that 233 mAh/g in the 3D SnS_2 QDs/rGO electrode, as presented in Fig. 4f. A serious capacity decay of the pure SnS_2 electrode can result from the low electronic conductivity of the unsupported SnS_2 and the uncontrollable aggregations of Sn (or its discharge products) during the cycling. Thus, the outstanding electrochemical performance of the electrode corresponds to the 3D honeycomb-like structure. The existing porous in the structure can efficiently adjust the volume change in the process of alloying and de-alloying.

To better understand the charge storage process, the CV curves at various scan rates (0.1–1 mV/s) are performed to understand the electrochemical process (Fig. 4g). A peak shift appears with the scanning rate rising from 0.1 to 1 mV/s, indicating the polarization of the electrode. The capacity contribution from capacitive and diffusion-controlled charge can be quantified according to the relation [51] $i(V) = k_1 v + k_2 v^{1/2}$, where $k_1 v$ and $k_2 v^{1/2}$ are the contributions from the capacitive and diffusion-controlled processes, respectively. From Fig. 4h, it can be observed that the capacitance-controlled capacity accounts for 76.1% of the total charge storage at a scan rate of 1 mV/s. With the scan rate increases in the order of 0.1, 0.3, 0.6, 0.7, and 1 mV/s, the proportion of the capacitance-controlled process increases from 67.4, 70.3, 73.2, 75.7, to 76.1%,

respectively (Fig. 4i). The result indicates that the capacitive charge storage plays an important role in the total capacity of the electrode [52]. However, the relative rapid capacity decreases at higher scan rate is attributed to the diffusion-limited electrochemical energy conversion process [53].

The structural advantages of the 3D SnS_2 QDs/rGO composite in LIBs and SIBs can be summarized as follows (Fig. 5): (i) the 3D structure can buffer the volume expansion and inhibit the agglomeration of SnS_2 QDs during the charge/discharge process. (ii) The 3D honeycomb-like porous structure can provide sufficient space for electrolyte storage. (iii) The 3D interconnected network is beneficial for enhancing electron conductivity and allowing the electron to transfer quickly in the continuous paths. (iv) The SnS_2 QDs with a particle size about ~ 6 nm can shorten the diffusion distance of Li^+/Na^+, resulting in good electrochemical performance.

Conclusions

A novel 3D honeycomb-like SnS_2 QDs/rGO composite was synthesized by one-pot spray drying and sulfidation. The SnS_2 QDs (~ 6 nm) was uniformly distributed in the rGO layers. The thicknesses of the rGO sheets could be regulated by changing the concentration of GO in the spray solution. What is more, the size of the rGO nanovoids could be easily adjusted by using different size of the PS nanospheres. The 3D honeycomb-like rGO could not only buffer the volume expansion of the SnS_2 QDs but also enhance their poor electrical conductivity. In addition, it can provide enough space for electrolyte reservoirs. As a result, the retention of the reversible capacity of the 3D SnS_2 QDs/rGO electrode for LIB at 0.1 A/g was nearly 862 mAh/g and the capacity was as high as 622 mAh/g after 200 cycles at 0.5 A/g. Moreover, a capacity of 233 mAh/g could be delivered after 200 cycles at 0.5 A/g in the SIB test. The novel 3D
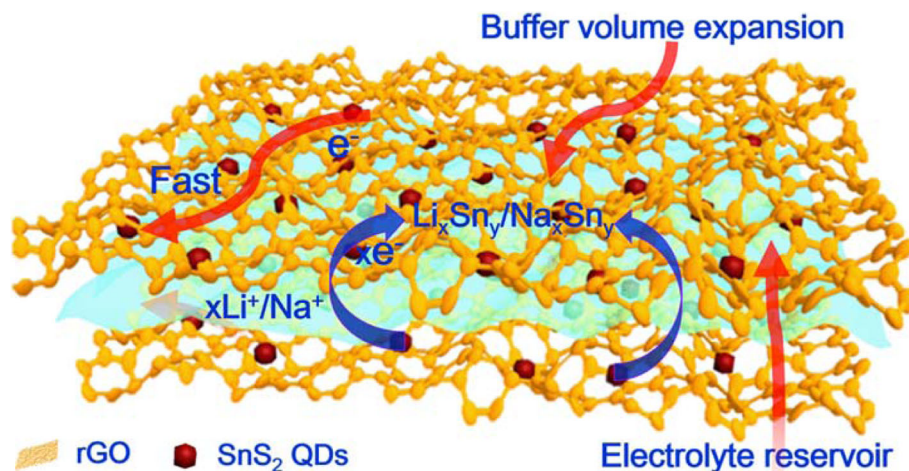
Fig. 5 Schematic illustration highlights the structural benefits of the 3D SnS_2 QDs/rGO composite during the charge/discharge process

honeycomb-like SnS_2 QDs/rGO composite suggested a new strategy for preparing anode material in LIBs and SIBs. This advanced anode materials is predicable to have a significant influence on the energy storage field, and thus, provide fresh opportunities to enhance the electrochemical performance of Li^+ and Na^+ storage devices.

Additional File

Additional file 1: Figure S1. a SEM image of the 3D SnO_2 /rGO composite. b TEM image of the 3D SnO_2 /rGO composite. c TEM image of the rGO backbone (after the removal of PS nanospheres). d TEM image of the rGO layer. **Figure S2.** a XRD pattern of the pure SnS_2 composite. **Figure S3.** Particle size distribution of 3D SnS_2 QDs/rGO after 200 charge/discharge cycles. **Figure S4a.** TGA curves of the 3D SnS_2 QDs/rGO composite under air flow with a temperature ramp of 10 °C min^{-1} from 30 °C temperature to 800 °C. (DOCX 2376 kb)

Abbreviations
3D SnS_2 QDs/rGO: 3D Honeycomb-like SnS_2 Quantum Dots/rGO; 3D: Three-dimensional; BET: The Brunauer–Emmett–Teller; CV: Cyclic voltammetry; DEC: Diethyl carbonate; EC: Ethylene carbonate; GO: Graphene oxide; LIBs: Lithium-ion batteries; PS: Polystyrene; SEI: Solid electrolyte interface; SEM: Field emission scanning electron microscope; SIBs: Sodium-ion batteries; TEM: Transmission electron microscope; TGA: Thermogravimetric analyzer; XPS: X-ray photoelectron spectroscopy; XRD: X-ray diffraction

Availability of Data and Materials
All data and materials are fully available without restriction.

Authors' Contributions
YG (Zhang) prepared the manuscript, YG and YG (Wang) carried out the experiment. TP, YL, RJ, and YB helped in the technical support for the characterizations. YS, XM, and JK designed the experiment. All the authors discussed the results and approved the final manuscript.

Competing Interests
The authors declare that they have no competing interests.

Publisher's Note
Springer Nature remains neutral with regard to jurisdictional claims in published maps and institutional affiliations.

Author details
[1]School of Physics and Electronic Engineering, Xinyang Normal University, Xinyang 464000, People's Republic of China. [2]Key Laboratory of Microelectronics and Energy of Henan Province, Xinyang Normal University, Xinyang 464000, People's Republic of China. [3]College of Chemistry and Chemical Engineering, Luoyang Normal University, Luoyang 471934, People's Republic of China. [4]Department of Mechanical and Aerospace Engineering, Hong Kong University of Science and Technology, Clear Water Bay, Kowloon, Hong Kong, People's Republic of China.

References
1. Du F, Li B, Fu W, Xiong Y, Wang K, Chen J (2014) Surface binding of polypyrrole on porous silicon hollow nanospheres for li-ion battery anodes with high structure stability. Adv Mater 26:6145–6150
2. Wu Z, Ren W, Wen L, Gao L, Zhao J, Chen Z, Zhou G, Cheng H (2010) Graphene anchored with Co_3O_4 nanoparticles as anode of lithium ion batteries with enhanced reversible capacity and cyclic performance. ACS Nano 4:3187–3194
3. Peng T, Liu C, Hou X, Zhang Z, Wang C, Yan H, Lu Y, Liu X, Luo Y (2017) Control growth of mesoporous nickel tungstate nanofiber and its application as anode material for lithium-ion batteries. Electrochim Acta 224:460–467
4. Luo Y, Luo J, Jiang J, Zhou W, Yang H, Qi X, Zhang H, Fan H, Yu D, Li C, Yu T (2012) Seed-assisted synthesis of highly ordered $TiO_2@\alpha$-Fe_2O_3 core/shell arrays on carbon textiles for lithium-ion battery applications. Energy Environ Sci 5:6559–6566
5. Jiang Z, Wang C, Du G, Zhong Y, Jiang J (2012) In situ synthesis of SnS_2@graphene nanocomposites for rechargeable lithium batteries†. J Mater Chem 22:9494–9496
6. Choi S, Ko Y, Lee J, Kang Y (2015) 3D MoS_2-graphene microspheres consisting of multiple nanospheres with superior sodium ion storage properties. Adv Funct Mater 25:1780–1788
7. Zhang Q, Wang J, Dong J, Ding F, Li X, Zhang B, Yang S, Zhang K (2015) Facile general strategy toward hierarchical mesoporous transition metal oxides arrays on three-dimensional macroporous foam with superior lithium storage properties. Nano Energy 13:77–91
8. Chen Z, Ren W, Gao L, Liu B, Pei S, Cheng H (2011) Three-dimensional flexible and conductive interconnected graphene networks grown by chemical vapour deposition. Nat Mater 10:424–428
9. Choi B, Yang M, Hong W, Choi J, Huh Y (2012) 3D macroporous graphene frameworks for supercapacitors with high energy and power densities. ACS Nano 6:4020–4028
10. Luo J, Kim J, Huang J (2013) Material processing of chemically modified graphene: some challenges and solutions. Acc Chem Res 46:2225–2234
11. Li C, Shi G (2012) Three-dimensional graphene architectures. Nanoscale 4: 5549–5563
12. Cao X, Zheng B, Rui X, Shi W, Yan Q, Zhang H (2014) Metal oxide-coated three-dimensional graphene prepared by the use of metal-organic frameworks as precursors†. Angew Chem 126:1428–1433
13. Huang Y, Wu D, Wang J, Han S, Lv L, Zhang F, Feng X (2014) Amphiphilic polymer promoted assembly of macroporous graphene/ SnO_2 frameworks with tunable porosity for high-performance lithium storage. Small 10:2226–2232
14. Choi S, Kang Y (2014) Crumpled graphene-molybdenum oxide composite powders: preparation and application in lithium-ion batteries. ChemSusChem 7:523–528
15. Zhu S, Li J, Deng X, He C, Liu E, He F, Shi C, Zhao N (2017) Ultrathin-nanosheet-induced synthesis of 3D transition metal oxides networks for lithium ion battery anodes. Adv Funct Mater 27:1605017
16. Deng Z, Jiang H, Hu Y, Liu Y, Zhang L, Liu H, Li C (2017) 3D ordered macroporous MoS_2@C nanostructure for flexible li-ion batteries. Adv. Mater 29:1603020
17. Choi S, Kang Y (2015) Sodium ion storage properties of WS_2-decorated three-dimensional reduced graphene oxide microspheres. Nanoscale 7: 3965–3970
18. Li C, Zhang X, Wang K, Zhang H, Sun X, Ma Y (2015) Three dimensional graphene networks for supercapacitor electrode materials. New Carbon Mater 30:193–206
19. Cao X, Yin Z, Zhang H (2014) Three-dimensional graphene materials: preparation, structures and application in supercapacitors. Energy Environ Sci 7:1850–1865
20. Xu Y, Shi G, Duan X (2015) Self-assembled three-dimensional graphene macrostructures: synthesis and applications in supercapacitors. Acc Chem Res 48:1666–1675

21. Zhou X, Wu T, Hu B, Yang G, Han B (2010) Synthesis of graphene/polyaniline composite nanosheets mediated by polymerized ionic liquid. Chem Commun 46:3663–3665
22. Hummer W, Offeman R (1958) Preparation of graphitic oxide. J Am Chem Soc 80:1339–1339
23. Choi S, Kang Y (2014) Synthesis for yolk-shell-structured metal sulfide powders with excellent electrochemical performances for lithium-ion batteries. Small 10:474–478
24. Chang K, Wang Z, Huang G, Li H, Chen W, Lee J (2012) Few-layer SnS_2/graphene hybrid with exceptional electrochemical performance as lithium-ion battery anode. J Power Sources 201:259–266
25. Yu Z, Li X, Yan B, Xiong D, Yang M, Li D (2017) Rational design of flower-like tin sulfide @ reduced graphene oxide for high performance sodium ion batteries. Mater. Res. ES Bull 96:516–523
26. Bian X, Lu X, Xue Y, Zhang C, Kong L, Wang C (2013) A facile one-pot hydrothermal method to produce SnS_2/reduced graphene oxide with flake-on-sheet structures and their application in the removal of dyes from aqueous solution. J colloid interf Sci 406:37–43
27. Yuan Y, Chen D, Shi X, Tu J, Hu B, Yang N, Yu Z, Zou Z (2017) Facile fabrication of "green" SnS_2 quantum dots/reduced graphene oxide composites with enhanced photocatalytic performance. Chem Eng J 313:1438–1446
28. Zhai C, Du N, Zhang H, Yu J, Yang D (2011) Multiwalled carbon nanotubes anchored with SnS_2 nanosheets as high-performance anode materials of lithium-ion batteries. ACS Appl Mater Interfaces 3:4067–4074
29. Hou X, Peng T, Cheng J, Yu Q, Luo R, Lu Y, Liu X, Kim J, He J, Luo Y (2017) Ultrathin ZnS nanosheet/carbon nanotube hybrid electrode for high-performance flexible all-solid-state supercapacitor. Nano Res 10:2570–2583
30. Li K, Yan S, Lin Z, Dai X, Qu P (2016) Preparation and lithium ion batteries properties of SnS_2 nanoparticle/reduced graphene oxide nanosheet nanocomposites using supercritical carbon dioxide. Synthetic Met 217:138–143
31. Zhang Y, Li J (2011) An improvement method of fractional-order filter approximation. Sep Purif Technol 81:101–106
32. Choi S, Kang Y (2015) Three-dimensional reduced graphene oxide microspheres. Nanoscale 7:3965–3970
33. Zhang Q, Li R, Zhang M, Zhang B, Gou X (2014) SnS_2/reduced graphene oxide nanocomposites with superior lithium storage performance. Electrochimi Acta 115:425–433
34. Zhang M, Lei D, Yu X, Chen L, Li Q, Wang Y, Wang T, Cao G (2012) Graphene oxide oxidizes stannous ions to synthesize tin sulfide-graphene nanocomposites with small crystal size for high performance lithium ion batteries. J Mater Chem 22:23091–23097
35. Kim H, Chung Y, Kang S, Sung Y (2009) Electrochemical behavior of carbon-coated SnS_2 for use as the anode in lithium-ion batteries. Electrochim Acta 54:3606–3610
36. Wang G, Shen X, Yao J, Park J (2009) Graphene nanosheets for enhanced lithium storage in lithium ion batteries. Carbon 47:2049–2053
37. Guo X, Fang X, Sun Y, Shen L, Wang Z, Chen L (2013) Lithium storage in carbon-coated SnO_2 by conversion reaction. J Power Sources 226:75–81
38. Tang H, Qi X, Han W, Ren L, Liu Y, Wang X, Hong J (2015) SnS_2 nanoplates embedded in 3D interconnected graphene network as anode material with superior lithium storage performance. Appl Surf Sci 355:7–13
39. Luo B, Fang Y, Wang B, Zhou J, Song H, Zhi L (2012) Two dimensional graphene-SnS_2 hybrids with superior rate capability for lithium ion storage†. Energy Environ Sci 5:5226–5230
40. He M, Yuan L, Huang Y (2013) Acetylene black incorporated three-dimensional porous SnS_2 nanoflowers with high performance for lithium storage. RSC Adv 3:3374–3383
41. Yin J, Cao H, Zhou Z, Zhang J, Qu M (2012) SnS_2@reduced graphene oxide nanocomposites as anode materials with high capacity for rechargeable lithium ion batteries†. J Mater Chem 22:23963–23970
42. Li J, Wu P, Lou F, Zhang P, Tang Y, Zhou Y, Lu T (2013) Mesoporous carbon anchored with SnS_2 nanosheets as an advanced anode for lithium-ion batteries. Electrochim Acta 111:862–868
43. Shen C, Ma L, Zheng M, Zhao B, Qiu D, Pan L, Cao J, Shi Y (2012) Synthesis and electrochemical properties of graphene-SnS_2 nanocomposites for lithium-ion batteries. J Solid State Electrochem 16:1999–2004
44. Ji L, Xin H, Kuykendall T, Wu S, Zheng H, Rao M, Cairns E, Battagliac V, Zhang Y (2012) SnS_2 nanoparticle loaded graphene nanocomposites for superior energy storage. Phys Chem Chem Phys 14:6981–6986
45. Sathish M, Mitani S, Tomai T, Honma I (2012) Ultrathin SnS_2 nanoparticles on graphene Nanosheets: synthesis, characterization, and li-ion storage applications. J Phys Chem C 116:12475–12481
46. Fan L, Li X, Song X, Hu N, Xiong D, Koo A, Sun X (2018) Promising dual-doped graphene aerogel/SnS_2 nanocrystal building high performance sodium ion batteries. ACS Appl Mater Interfaces 10:2637–2648
47. Zhou P, Wang X, Guan W, Zhang D, Fang L, Jiang Y (2017) SnS_2 nanowall arrays toward high performance sodium storage. ACS Appl Mater Interfaces 9:6979–6987
48. Wang J, Luo C, Mao J, Zhu Y, Fan X, Gao T, Mignerey A, Wang C (2015) Solid-state fabrication of SnS_2/C nanospheres for high-performance sodium ion battery anode. ACS Appl Mater Interfaces 7:11476–11481
49. Wu L, Hu X, Qian J, Pei F, Wu F, Mao R, Ai X, Yang H, Cao Y (2013) A Sn-SnS-C nanocomposite as anode host materials for Na-ion batteries. J Mater Chem A 1:7181–7184
50. Xu W, Zhao K, Zhang L, Xie Z, Cai Z, Wang Y (2016) SnS_2@graphene nanosheets arrays grown on carbon cloth as freestanding binder-free flexible anodes for advanced sodium batteries. J. Alloys Compd 654:357–362
51. Brezesinski T, Wang J, Tolbert S, Dunn B (2010) Ordered mesoporous α-MoO_3 with iso-oriented nanocrystalline walls for thin-film pseudocapacitors. Nat Mater 9:146–151
52. Xu R, Wang G, Zhou T, Zhang Q, Cong H, Xin S, Rao J, Zhang C, Liu Y, Guo Z, Yu S (2017) Rational design of Si@carbon with robust hierarchically porous custard-apple-like structure to boost lithium storage. Nano Energy 39:253–261
53. Xiong X, Yang C, Wang G, Lin Y, Qu X, Wang J, Zhao B, Liu B, Lin Z, Huang K (2017) SnS nanoparticles electrostatically anchored on three dimensional N-doped graphene as an active and durable anode for sodium ion batteries. Energy Environ Sci 10:1757–1763